Supplementary Information
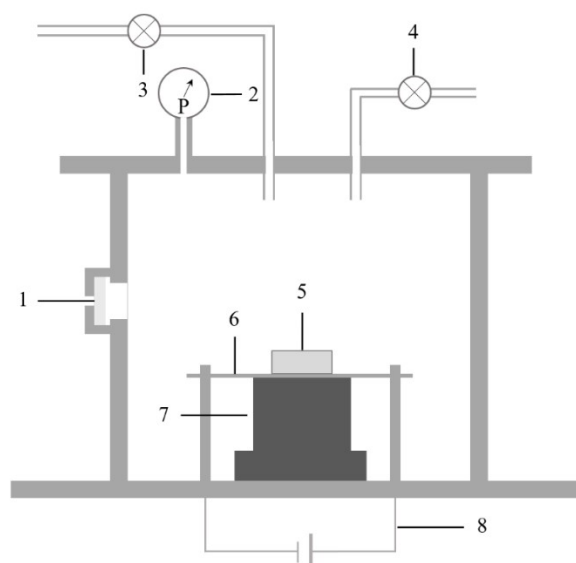
AlN micro-honeycomb reinforced stearic acid-based phase-change composites with high thermal conductivity for solar-thermal-electric conversion

Jiabin Hu, Zhilei Wei, Bangzhi Ge, Lei Zhao, Kang Peng, Zhongqi Shi [*]

State Key Laboratory for Mechanical Behavior of Materials, Xi'an Jiaotong

University, Xi'an 710049, China

E-mail: zhongqishi@mail.xjtu.edu.cn (Z Shi)

**Fig. S1** Schematic for the home-made combustion synthesis furnace

The schematic of the home-made combustion synthesis furnace is shown in **Fig. S1**, where 1—Observation window; 2—Pressure gauge; 3—Inlet valve; 4—Vacuum valve; 5—Sample; 6—Graphite paper stripe; 7—Base support; 8—Power supply.
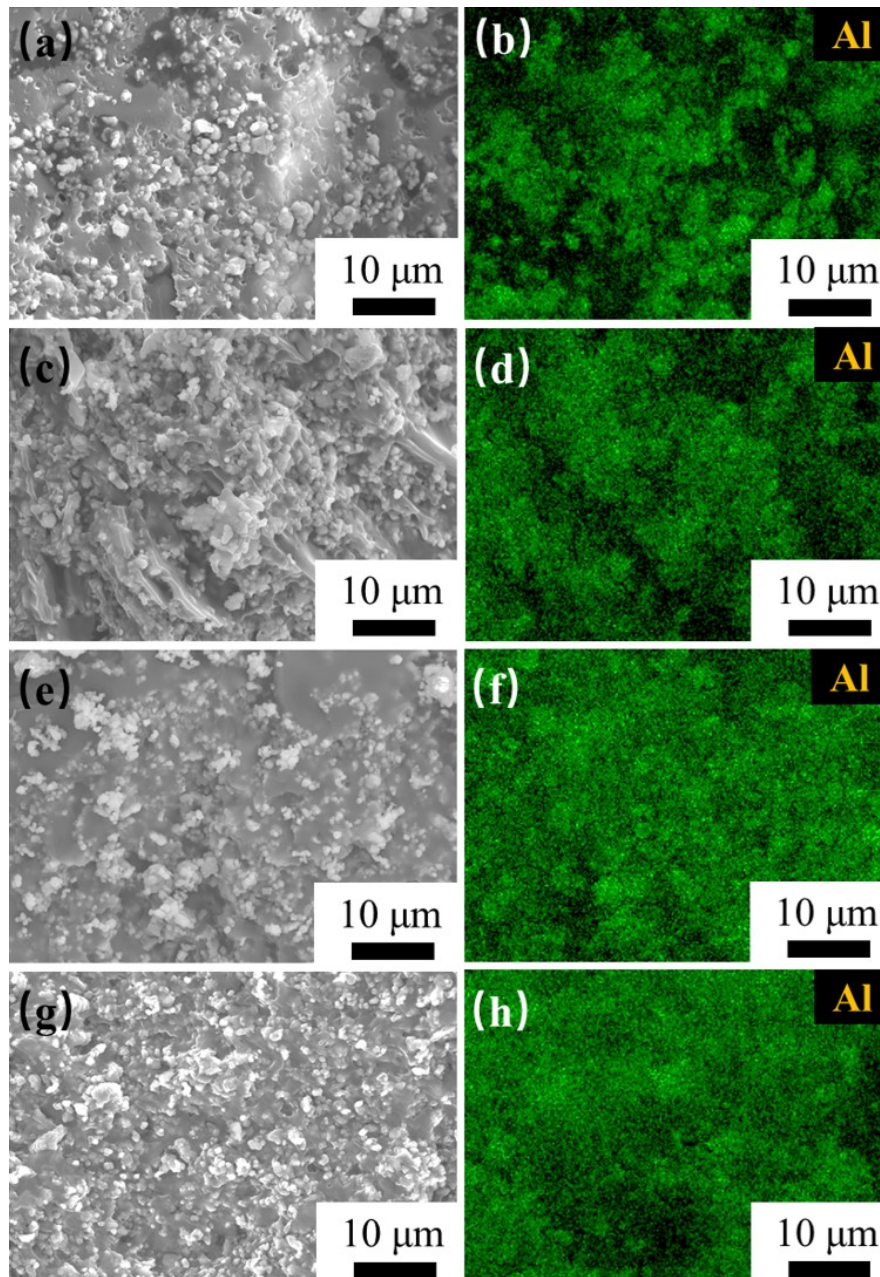
Fig. S2 Side-view fracture morphologies and corresponding EDS results of Al element of the RD-AlN/SA composites with different solid loadings: (a), (b) 11.77 vol%; (c), (d) 17.10 vol%; (e), (f) 26.15 vol%; (g), (h) 35.59 vol%

The detailed data processing of EMT fitting: To predigest the calculating process, the Eq. **(4)** in the paper was converted to $y = (0.768 + 0.256Ax)/(3 - Bx)$, where $\beta_1 + \beta_2$ equals to A; β_2 equals to B; x and y are denoted as V_f and K_c, respectively. The

effective medium theory (EMT) fitting result is demonstrated in **Fig. S3**, and the calculated β_1 and R_{c1} for the RD-AlN/SA composite are presented in **Table S1**.
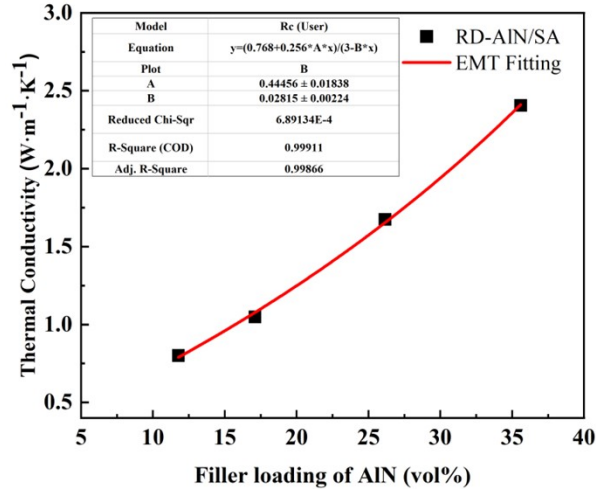

Fig. S3 EMT fitting curve of the RD-AlN/SA composites

Table S1 The calculated β_1 and R_{c1} values for the RD-AlN/SA composites

Composite type	β_1	R_{c1} ($m^2 \cdot K \cdot W^{-1}$)
RD-AlN/SA	0.42	6.36×10^{-7}

The detailed data processing of nonlinear Foygel fitting: In this work, a (the aspect ratio) and V_c (the critical percolation volume fraction of filler) were taken as ~1 and 1.2, respectively. To simplify the calculating process, the Eq. **(6)** in the paper was transformed to $y = Ax + B$, where y stands for $\log(K_c - K_m)$; x represents $\log[(V_f - V_c)/(1 - V_c)]$; A and B are γ and $\log\lambda_0$, respectively. The nonlinear Foygel fitting results are demonstrated in **Fig. S4**, and the calculated A, B, γ and λ_0 values for the RD-AlN/SA composites and the MH-AlN/SA composites at parallel and perpendicular to the channel directions are presented in **Table S2**.
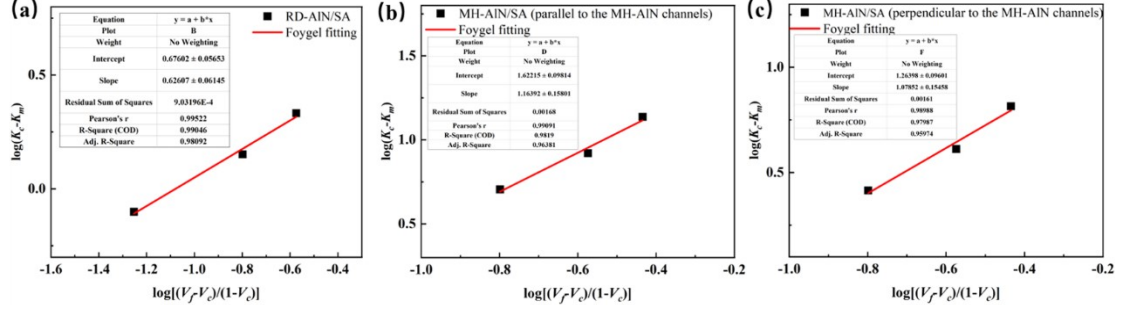
Fig. S4 Nonlinear Foygel fitting curves for: (a) the RD-AlN/SA composites; (b) the MH-AlN/SA composites in the directions parallel to the MH-AlN channels and (c) the MH-AlN/SA composites in the directions perpendicular to the MH-AlN channels.

Table S2 The calculated A, B, γ and λ_0 values for the RD-AlN/SA composites, the MH-AlN/SA (perpendicular to the MH-AlN channels) composites and MH-AlN/SA (parallel to the MH-AlN channels) composites.

Composite type	A	B	γ	λ_0
RD-AlN/SA	0.63	4.74	0.63	4.74
MH-AlN/SA (perpendicular to the MH-AlN channels)	1.08	1.26	1.08	18.36
MH-AlN/SA (parallel to the MH-AlN channels)	1.16	1.62	1.16	41.89

The interfacial thermal resistance (R_{c2}) between the AlN particles can be obtained by combination of the Eq. **(S1)** and Eq. **(S2)** [1]:

$$R = 1 / [\lambda_0 d(V_c)^\gamma] \tag{S1}$$

$$R_{c2} = R \times S \tag{S2}$$

where S is the overlapped area of two AlN particles. In this work, it is assumed that

1/100 of each AlN surface (~4.91×10^{-14} m^2) involves in the heat transfer of the interconnected AlN network [2].

According to the fitting results, the calculated R_{c2} values for the RD-AlN/SA composites, the MH-AlN/SA (perpendicular to the MH-AlN channels) composites and the MH-AlN/SA (parallel to the MH-AlN channels) composites are 1.55×10^{-8} m$^2\cdot$K$\cdot$W^{-1}, 1.03×10^{-8} m$^2\cdot$K$\cdot$W^{-1} and 5.42×10^{-9} m$^2\cdot$K$\cdot$W^{-1}, respectively.

Table S3 The thermophysical properties of pure SA and the MH-AlN/SA composites.

Sample	[a]T_m (°C)	[b]ΔH_m (J·g^{-1})	[c]T_c (°C)	[d]ΔH_c (J·g^{-1})
Pure SA	68.8	220.5	65.2	222.1
11.77MH-AlN/SA	66.8	126.2	66.5	130.3
17.10MH-AlN/SA	66.7	116.5	65.7	117.6
26.15MH-AlN/SA	68.6	79.8	65.7	80.8
35.59MH-AlN/SA	67.3	57.2	63.9	64.0
44.46MH-AlN/SA	67.6	41.4	64.7	45.4

[a]Melting temperature.

[b]Latent heat of fusion.

[c]Freezing temperature.

[d]Latent heat of solidification.

**Table S4** Thermal conductivity and latent heat of ceramic-based phase-change composites.

PCM	Additives	K_{PCM} (W·m^{-1}·K^{-1})	Fraction of additives	K_{PCC} (W·m^{-1}·K^{-1})	LH (J·g^{-1})	Ref.
PEG	β-AlN/SiO$_2$	0.30	20.0 wt%	0.57	129.5	[3]
SA-ODE	h-BN	0.30	15.0 wt%	0.33	189.1	[4]
CH$_3$COONa ·3H$_2$O	h-BN	0.74	5.0 wt%	1.20	210.0	[5]
PEG	BN/GNP	0.31	31.0 wt%	1.33	122.2	[6]
Paraffin	h-BN	0.12	26.0 wt%	1.33	135.1	[7]
LA-PA-SA	Expanded perlite	0.44	45.0 wt%	0.86	81.5	[8]
CA	Expanded perlite/EG	0.09	55.0 wt%	0.14	96.3	[9]
PEG	BN/GO	0.32	19.2 wt%	1.84	145.9	[10]
PEG	BN/GO	0.33	28.7 wt%	3.18	143.6	[11]
PEG	BN/GO	0.33	23.0 wt%	2.36	138.2	[12]
SA	Bentonite/Graphite	0.26	30.0 wt%	0.77	84.6	[13]
SA	EV	0.34	36.9 wt%	0.52	134.3	[14]
PEG	Ag/Diatomite	0.36	37.0 wt%	0.82	111.3	[15]
CA	Graphite/Halloysite	0.2	40.0 wt%	0.76	75.5	[16]
Paraffin	Kaolinite	0.25	49.1 wt%	0.78	94.8	[17]
SA	AlN	0.26	26.2 vol%	5.33	80.8	This work

K_{PCM}: thermal conductivity of the pure phase-change material.

K_{PCC}: thermal conductivity of the phase-change composite.

LH: latent heat of the phase-change composite.

Fig. S5 depicts the digital photos of the thermoelectric generator. The device designed for the solar-thermal-electric conversion comprises a Fresnel lens, the 44.46MH-AlN/SA phase-change composite, a thermoelectric plate and metal-based heat sink. At first, the Fresnel lens was fixed at a proper angle and help the solar light converge on the surface of the 44.46MH-AlN/SA composite. Notably, the composite was coated with a thin film of graphite to convert solar energy into thermal energy via photothermal effect. Owing to the excellent thermal conduction performance of the composite, the heat can be transfer quickly within the as-prepared composite so that thermal energy can be distributed homogeneously throughout the as-prepared composite and stored in the form of latent heat when SA melts. The composite was in close contact with the thermoelectric plate ($20 \times 20 \times 2$ mm) which could convert the thermal energy into the electric energy by the temperature gradient between heat source and heat sink, and ice was placed around the heat sink to increase the temperature difference. Additionally, a thermal-conductive silicon sheet was used to lower the interfacial thermal resistance between the composite and the thermoelectric plate. Finally, the output current and voltage were recorded by the multimeter.
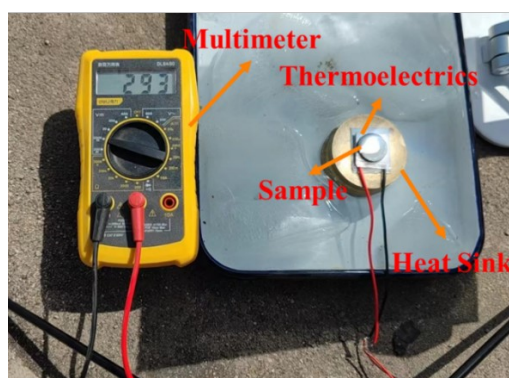
Fig. S5 Digital photo of the thermoelectric generator

Table S5 Comparison in the output voltage and peak output power density of the PCM-based solar-thermal-electric devices in the previous research.

PCM	Additives	Solar irradiation power $(W \cdot m^{-2})$	Output voltage (mV)	Output current (mA)	Output Power density $(W \cdot m^{-2})$	Ref.
OM$_{35}$	Al$_2$O$_3$	690	615.0	84.9	32.6	[18]
PEG	BN	780	251.0	64.2	40.3	[19]
PEG	BN/GO	8000	200.0	45.0	5.6	[10]
PEG	BN/GNP	8000	130.0	27.5	2.2	[6]
D-mannitol	Polybenzobisoxazole fiber	780	3410.0	191.0	198.7	[20]
m-PEGMA	GO	2000	144.0	14.8	-	[21]
SA	AlN	740	409.0	110.8	113.3	This work

References：

1. J. Ma, T. Shang, L. Ren, Y. Yao, T. Zhang, J. Xie, B. Zhang, X. Zeng, R. Sun, J. Xu and C. P. Wong, *Chem. Eng. J.*, 2020, **380**, 122550.
2. X. Zeng, Y. Yao, Z. Gong, F. Wang, R. Sun, J. Xu and C. P. Wong, *Small*, 2015, **11**, 6205-6213.
3. W. Wang, X. Yang, Y. Fang, J. Ding and J. Yan, *Appl. Energy*, 2009, **86**, 1196-1200.
4. D. Su, Y. Jia, G. Alva, F. Tang and G. Fang, *Energy Buildings*, 2016, **131**, 35-41.
5. M. Fashandi and S. N. Leung, *Sol. Energy Mater. Sol. Cells*, 2018, **178**, 259-265.
6. J. Yang, L. Tang, R. Bao, L. Bai, Z. Liu, W. Yang, B. Xie and M. Yang, *Chem. Eng. J.*, 2017, **315**, 481-490.
7. Z. Qian, H. Shen, X. Fang, L. Fan, N. Zhao and J. Xu, *Energy Buildings*, 2018, **158**, 1184-1188.
8. N. Zhang, Y. Yuan, Y. Yuan, T. Li and X. Cao, *Energy Buildings*, 2014, **82**, 505-511.
9. A. Sari and A. Karaipekli, *Mater. Chem. Phys.*, 2008, **109**, 459-464.
10. J. Yang, L. Tang, R. Bao, L. Bai, Z. Liu, W. Yang, B. Xie and M. Yang, *J. Mater. Chem. A*, 2016, **4**, 18841-18851.
11. J. Yang, L. Tang, L. Bai, R. Bao, Z. Liu, B. Xie, M. Yang and W. Yang, *ACS Sustainable Chem. Eng.*, 2018, **6**, 6761-6770.
12. C. Li, L. Fu, J. Ouyang, A. Tang and H. Yang, *Appl. Clay Sci.*, 2015, **115**, 212-220.
13. J. Yang, P. Yu, L. Tang, R. Bao, Z. Liu, M. Yang and W. Yang, *Nanoscale*, 2017, **9**, 17704-17709.
14. C. Li, L. Fu, J. Ouyang and H. Yang, *Sci. Rep.*, 2013, **3**, 1908.

15. X. Zhang, Z. Yin, D. Meng, Z. Huang, R. Wen, Y. Huang, X. Min, Y. Liu, M. Fang and X. Wu, *Renewable Energy*, 2017, **112**, 113-123.

16. T. Qian, J. Li, X. Min, W. Guan, Y. Deng and L. Ning, *J. Mater. Chem. A*, 2015, **3**, 8526-8536.

17. D. Mei, B. Zhang, R. Liu, Y. Zhang and J. Liu, *Sol. Energy Mater. Sol. Cells*, 2011, **95**, 2772-2777.

18. Y. Jeyashree, Y. Sukhi, A. Vimala Juliet, S. Lourdu Jame and S. Indirani, *Mater. Sci. Semicond. Process.*, 2020, **107**.

19. D. Liu, C. Lei, K. Wu and Q. Fu, *ACS Nano*, 2020, **14**, 15738-15747.

20. Y. Zhang, K. Wu and Q. Fu, *Adv. Funct. Mater.*, 2021, **32**, 2109255.

21. R. Cao, D. Sun, L. Wang, Z. Yan, W. Liu, X. Wang and X. Zhang, *J. Mater. Chem. A*, 2020, **8**, 13207-13217.